INORGANIC CHEMISTRY FRONTIERS

RESEARCH ARTICLE

View Article Online
View Journal | View Issue

Cite this: *Inorg. Chem. Front.*, 2025, **12**, 561

Steric effect-induced modulation of crystallographic symmetry: implementing ferroelasticity in molecular ferroelectrics†

Jie Yao,‡[a] Zi-Jie Feng,‡[a] Jin-Qi Hu,‡[a] Guo-Wei Du,[a] Yu-An Xiong,[a] Hao-Ran Ji,[a] Tai-Ting Sha,[a] Xiangzhi Zhang,[b] Zheng-Yin Jing,[a] Qiang Pan,*[a] Huihui Hu*[a] and Yu-Meng You*[a]

Received 8th October 2024,
Accepted 9th November 2024

DOI: 10.1039/d4qi02527j

rsc.li/frontiers-inorganic

Ferroelastic materials, as a significant category of primary ferroic materials, have paved the way for the development of shape memory, superelasticity, tunable electronics, MEMS and actuators. The ferroic phase transition rules summarized by Aizu provide a theoretical guideline for material design. However, ferroelectrics and ferroelastics are to some extent intertwined with each other. Decoupling these properties is essential for optimizing material performance and developing better theoretical models. By modifying $[(CH_3)_4N][FeCl_4]$, a typical molecular ferroelectric that is not ferroelastic, we synthesized $(Me_2EtNCH_3CH_2Cl)FeCl_4$ (DMCE-$FeCl_4$), an organic–inorganic hybrid compound that introduces ferroelasticity while maintaining ferroelectricity. DFT calculations reveal that the shape of the organic cations contributes to ferroelasticity, while their dipole moments contribute to ferroelectricity. This work advances the understanding of ferroic properties and their independent control, with implications for reconfigurable memory devices and intelligent actuators.

Introduction

Since ferroelasticity was first observed in $Gd_2(MoO_4)_3$ in 1969,[1] ferroelastic materials, notably $BaTiO_3$ and $Bi_4Ti_3O_{12}$, have been extensively developed and utilized in many fields such as shape memory, superelasticity, tunable electronics, microelectromechanical systems (MEMS), and actuators.[2–6] In recent years, additional functionalities have been discovered in ferroelastic materials, including catalytic, controllable electronic and phonon transport properties.[7–9] Moreover, ferroelastic domain walls possess unique advantages, as their emerging properties are localized within domain walls, which are critical for applications in superconductivity and neuromorphic computation.[10–12] Consequently, the design and development of multifunctional ferroelastics are urgently required.

Over the past few decades, molecular materials have attracted increasing attention because of their unique advantages, including ease of preparation, structural flexibility, and high biocompatibility.[13–17] Several high-performance molecular ferroelastic materials have been found, such as $(cyclohexanemethylammonium)_2PbCl_4$ with a fully ferroelectric–full ferroelastic effect and high phase transition temperature[18] and $(Me_3NCH_2Cl)CdCl_3$ featuring fully-ferroelectric/partially ferroelastic species with large d_{33}.[19] The adjustability of components offers significant opportunities for chemical design aimed at optimizing the performance of molecular materials. However, most research actually aims at introducing ferroelectric polarization, while ferroelasticity often emerges as an incidental outcome.

From a theoretical perspective, ferroelectrics and ferroelastics are to some extent intertwined with each other. Ferroelectricity and ferroelasticity are both a consequence of symmetry breaking in structural phase transitions.[20–23] Aizu has cataloged the possible types of ferroelectric and ferroelastic phase transitions.[24,25] Among the 94 ferroelastic transitions, 42 also belong to ferroelectric transitions. Therefore, for most molecular materials, their ferroelectricity and ferroelasticity have a high probability of coupling, which makes it difficult to study the mechanism of each individual property from the perspective of chemical design. Decoupling allows for the independent optimization of multiple properties and better theoretical models by reducing the complexity of systems and understanding the individual contributions of different variables.[26–30] Consequently, a new molecular

[a]*Jiangsu Key Laboratory for Science and Applications of Molecular Ferroelectrics, Southeast University, Nanjing 211189, People's Republic of China.*
E-mail: youyumeng@seu.edu.cn, huhuihui@seu.edu.cn, pq@seu.edu.cn
[b]*College of Chemistry and Materials Science, Shanghai Normal University, Shanghai, 200234, China*

† Electronic supplementary information (ESI) available. CCDC 2380776–2380778. For ESI and crystallographic data in CIF or other electronic format see DOI: https://doi.org/10.1039/d4qi02527j

‡ These authors contributed equally to this work.

material, with ferroelectric–ferroelastic decoupling, is urgently needed to clarify the fundamental differences between ferroelastic and ferroelectric properties.

Herein, we start with $[(CH_3)_4N][FeCl_4]$,[31,32] a typical molecular ferroelectric that is not ferroelastic. By modifying the tetramethylammonium cation, we synthesized an organic–inorganic hybrid semiconductor, $(Me_2EtNCH_3CH_2Cl)FeCl_4$ (DMCE-$FeCl_4$), which introduces ferroelasticity while retaining ferroelectricity. The order–disorder motions of the $[DMCE]^+$ cations are accompanied by two lattice evolutions: DMCE-$FeCl_4$ experiencing a ferroelastic transition (6*mmFmm*2) at 299.9 K (T_{C1}) and a ferroelectric transition (6/*mmmF*6*mm*) at 409.2 K (T_{C2}). According to DFT calculations, the shape of the organic cations contributes to the ferroelasticity, while the dipole and displacement of the organic cations contribute to the ferroelectricity. Through precise chemical design, the ferroelectricity and ferroelasticity can be regulated independently. This work is anticipated to enhance our understanding of the relationship between ferroelectrics and ferroelastics and to inspire applications in reconfigurable memory devices, intelligent actuators, and adaptive robotics.

Results and discussion

By modifying the tetramethylammonium cation, we synthesized an organic compound (dimethylchloroethylethyl) ammonium chloride (Fig. 1a). Yellow-green transparent crystals of DMCE-$FeCl_4$ were synthesized from a concentrated hydrogen chloride solution by employing a 1 : 1 molar ratio of $FeCl_3$ and (dimethylchloroethylethyl)ammonium chloride, followed by slow evaporation (see the ESI†). The powder X-ray diffraction (PXRD) patterns recorded at 303 K correlate well with the results simulated from the single-crystal structure at 303 K, indicating the phase purity of DMCE-$FeCl_4$ (Fig. S1†). Thermogravimetric analysis shows that the decomposition temperature of DMCE-$FeCl_4$ can reach up to 590 K (Fig. S2†). The crystal structures of DMCE-$FeCl_4$ were determined by single crystal X-ray diffraction at 263 K, 303 K and 423 K. At 263 K, DMCE-$FeCl_4$ crystallizes in an orthorhombic non-centrosymmetric space group of $Pca2_1$ (point group *mm*2), with unit cell parameters of a = 13.9417 Å, b = 7.5995 Å, c = 13.4141 Å, α = 90°, β = 90°, and γ = 90° (Table S1†). The asymmetric unit of DMCE-$FeCl_4$ is formed by a $[DMCE]^+$ cation and a $[FeCl_4]^-$ anion. As illustrated in Fig. 1b, the framework of the $[FeCl_4]^-$ anion adopts a tetrahedral geometry. The Fe–Cl bond lengths range from 2.183(3) to 2.195(2) Å, while the C–Cl bond length within the $[DMCE]^+$ cation measures 1.758 Å (Fig. S3a and S3d†). As the temperature rises to 303 K, DMCE-$FeCl_4$ crystallizes in a hexagonal non-centrosymmetric space group of $P6_3mc$ (point group 6*mm*), characterized by the unit cell parameters of $a = b$ = 8.0036 Å, c = 13.3130 Å, $\alpha = \beta$ = 90°, and γ = 120°. At this temperature, the $[DMCE]^+$ cations exhibit disorder, and the C–Cl bond length in the $[DMCE]^+$ cation is 1.70 Å (Fig. 1b). The framework of the $[FeCl_4]^-$ anion still adopts a tetrahedral geometry, with Fe–Cl bond lengths ranging from 2.192(9) to 2.199(6) Å. Notably, the ethyl group is positioned on the mirror plane and all the C–Cl bonds are orderly arranged along the crystallographic *c*-axis, resulting in spontaneous polarization along the [001] direction of the crystal (Fig. S3b and S3e†). With further structural determination at 423 K, DMCE-$FeCl_4$ crystallizes in a hexagonal centro-

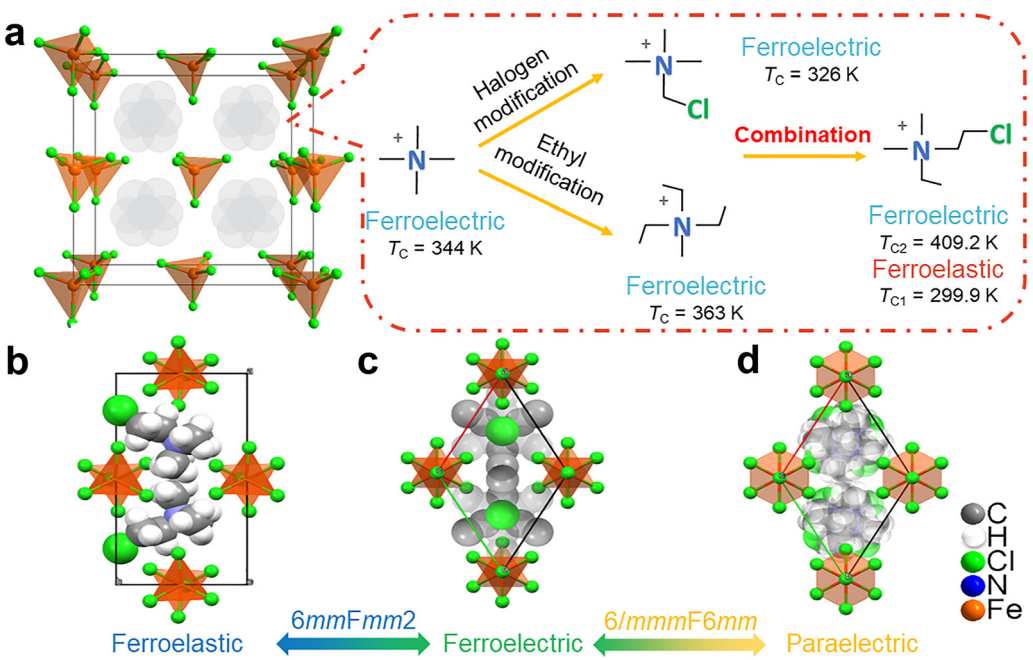

Fig. 1 (a) Design strategy of the molecular ferroelectric DMCE-$FeCl_4$ with multiple ferroic phase transitions. Perspective views along the *c*-axis at (b) 263 K, (c) 303 K, and (d) 423 K. H atoms bonded to the C atoms are omitted for clarity.

symmetric space group of $P6_3mmc$ (point group 6/*mmm*), with the unit cell parameters of a = 13.9417 Å, b = 7.5995 Å, c = 13.4141 Å, and $\alpha = \beta = \gamma = 90°$. At this temperature, $[DMCE]^+$ cations exhibit strongly disorder, with carbon atoms and chlorine atoms distributed across multiple equivalent orientations, rendering them indistinguishable (Fig. 1c). Similarly, the $[FeCl_4]^-$ anions exhibit highly disordered states along the 6-fold and 3-fold rotation axes to satisfy the crystal symmetry (Fig. S3c and S3f†). Variable-temperature PXRD measurement was conducted on DMCE-$FeCl_4$ from 303 K to 413 K (Fig. S4†). Upon heating from 303 to 393 K, the PXRD patterns show no obvious change. However, upon further heating above 403 K, most of the diffraction peaks disappear. The few remaining diffraction peaks suggest a higher crystal symmetry, consistent with the $P6_3mmc$ space group. Overall, the ferroelectricity of DMCE-$FeCl_4$ is attributed to an order–disorder mechanism. Crystal structure analysis reveals a phase transition at 299.9 K corresponding to the Aizu species 6*mmFmm*2, indicative of a ferroelastic phase transition, as well as a phase transition at 409.2 K associated with the Aizu species 6/*mmmF*6*mm*, which is linked to the ferroelectric phase transition.

In the differential scanning calorimetry (DSC) curves of DMCE-$FeCl_4$, two distinct pairs of peaks are observed at 299.9 K and 409.2 K during the heating process. DMCE-$FeCl_4$ exhibits a ferroelastic phase transition at 299.9 K and a relatively high ferroelectric phase transition at 409.2 K (Fig. 2a). Thermal hysteresis values of 10.8 K and 15.6 K occur at the phase transitions, which is characteristic of a first-order phase transition. For convenience, the three solid phases of DMCE-$FeCl_4$ are referred to as the low-temperature phase (LTP), intermediate-temperature phase (ITP) and high-temperature phase (HTP). During the heating process, the accompanying entropy changes (ΔS) for the phase transitions are about 22.57 J mol^{-1} K^{-1} and 12.67 J mol^{-1} K^{-1}, respectively. According to the Boltzmann equation, $\Delta S = R\ln(N)$, where R is the gas constant and N represents the possible orientation, the calculated N values are 15.09 and 4.59, respectively. These larger N values are related to the order–disorder motion of the $[DMCE]^+$ cation. Additionally, the temperature-dependent real part (ε') of the dielectric permittivity of DMCE-$FeCl_4$ displays a step-like dielectric anomaly near T_{C1} and T_{C2} (Fig. 2b), further confirming the occurrence of a phase transition in DMCE-$FeCl_4$.

The symmetry variation accompanying the phase transitions in DMCE-$FeCl_4$ was further investigated through the temperature dependence of the second harmonic generation (SHG) response. This method is effective for detecting the change from non-centrosymmetric to centrosymmetric inversion symmetry. As illustrated in Fig. 2c, DMCE-$FeCl_4$ exhibits SHG active behavior with an obvious signal below 409.2 K, indicating that its ITP crystallizes in a non-centrosymmetric space group, which aligns with the results of its structural analysis. As the temperature increases, the SHG signal rapidly diminishes to zero at 409 K, signifying a transition from a non-centrosymmetric structure to a centrosymmetric structure. In addition, the SHG intensity of DMCE-$FeCl_4$ exhibits anisotropy (Fig. 2d).

The ferroelectric polarization reversal was directly confirmed through measurements of the typical polarization–voltage (*P*–*V*) hysteresis loop. A thin film of DMCE-$FeCl_4$ was prepared using the drop-coating method on an indium tin oxide (ITO)-coated glass substrate (ESI Scheme 1†). The thin film of DMCE-$FeCl_4$ has a thickness of about 30 μm. The *P*–*V* hysteresis loops were obtained from the current density–

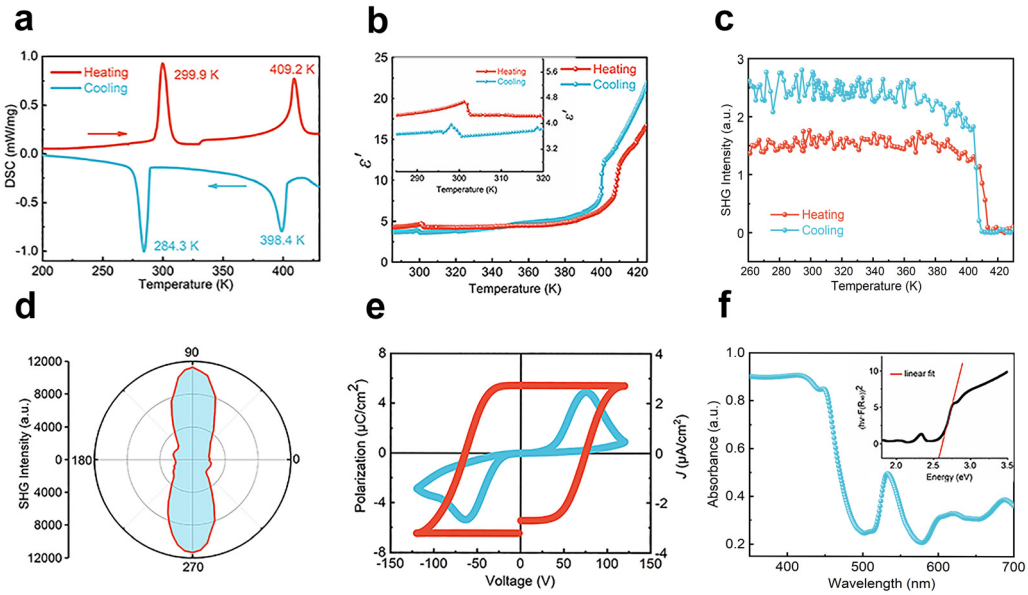

Fig. 2 (a) DSC curves of DMCE-$FeCl_4$ upon heating and cooling. (b) Variable-temperature PXRD measurement of DMCE-$FeCl_4$. (c) Temperature-dependent SHG response of DMCE-$FeCl_4$. (d) Polarization-dependent SHG plots collected for DMCE-$FeCl_4$. (e) *P*–*V* hysteresis loop of DMCE-$FeCl_4$ at room temperature. (f) UV–vis absorption spectra of DMCE-$FeCl_4$ (inset: Tauc plot; the estimated bandgap is 2.51 eV).

voltage (J–V) curves using the double-wave method. Based on the current accumulating data, a well-shaped P–V hysteresis loop is obtained, with a saturated polarization (P_s) and coercive voltage (V_c) of 5.5 μC cm^{-2} and 70 V, respectively (Fig. 2e).

To investigate the optical properties of DMCE-$FeCl_4$, UV–vis absorption spectra were recorded in the solid state at room temperature. As demonstrated in Fig. 2f, DMCE-$FeCl_4$ exhibits a steep absorption edge at around 500 nm, characteristic of direct bandgap semiconductors. The optical bandgap of DMCE-$FeCl_4$ was determined to be 2.51 eV using the Tauc plot (Fig. 2f, inset). This value is notably lower than those observed in several typical Pb-based and Cd-based molecular ferroelectrics, such as $((CH_3)_3NCH_2I)PbI_3$ (2.82 eV),[33] (benzylammonium)$_2PbCl_4$ (3.65 eV),[34] and (6-HBA)$_2CdBr_4$ (4.10 eV),[35] and even comparable with those of inorganic ferroelectric $BiFeO_3$ (2.7 eV)[36] and $Cs_3Bi_2I_9$ (2.0–3.5 eV).[37] Therefore, this provides an ideal nominator for the development of eco-friendly ferroelectric semiconductor devices.

In addition, we calculated the electronic band structure and partial density of states (PDOS) according to DFT. The energy band diagram reveals that the conduction band minimum (CBM) and the valence band maximum (VBM) are located at the same position in the Brillouin zone, confirming the presence of a direct bandgap (Fig. S5a†). This conclusion is consistent with the results obtained from UV–vis absorption spectroscopy. Due to the limitations inherent in DFT calculations, the bandgap was calculated to be 2.05 eV. As shown in Fig. S5b,† it is evident that the VBM primarily originates from the non-bonded Cl-3p orbitals, while the CBM mainly arises from the unoccupied Fe-3d and Cl-3p orbitals. Consequently, the bandgap of DMCE-$FeCl_4$ is determined by the inorganic $[FeCl_4]^-$ framework.

The piezoresponse force microscopy (PFM) technique is an indispensable technique that enables nondestructive imaging and manipulation of ferroelectric domains at the nanoscale. We obtained vertical and lateral PFM amplitude and phase images of the thin films of DMCE-$FeCl_4$ (Fig. 3a). As shown in Fig. 3b and c, the results reveal distinct phase contrasts and domain walls. In the PFM phase image, domains colored in purple and yellow exhibit a 180° contrast, indicating that the polarization directions of each domain are opposite. Notably, the irregular domain patterns did not align with the topography of the thin film. By comparing the PFM phase and amplitude images obtained in the lateral and vertical directions, it is inferred that DMCE-$FeCl_4$ behaves as a uniaxial ferroelectric, which is consistent with the results from crystal structure determination (Fig. 3b, c, e and 3f). The scanning SHG image corresponds well to the ferroelectric domain pattern, as shown in Fig. 3g, with the SHG signal at the domain wall being relatively weak. To further substantiate the ferroelectricity of DMCE-$FeCl_4$, we examined ferroelectric domain switching through PFM. We performed PFM switching spectroscopy at selected points on the thin film of DMCE-$FeCl_4$. The typical butterfly-shaped amplitude and hysteretic phase loops provide compelling evidence of ferroelectric switching in DMCE-$FeCl_4$ (Fig. 3i). Additionally, a 50 μm × 50 μm region of the film was chosen to visually verify polarization switching. As depicted in Fig. 3g and f, when an external voltage of −30 V was applied to the central region, the polarization was successfully switched. Conversely, by applying a bias of +30 V, the domain can also be flipped back (Fig. S6†). Importantly, during this domain manipulation, the surface morphology of the thin film remained unchanged, indicating that polarization switching is not influenced by the surface morphology (Fig. S6†). The results of the PFM measurement strongly confirm that DMCE-$FeCl_4$ possesses stable and switchable polarization.

The symmetry breaking of 6*mmFmm*2 species in T_{C1} indicates that DMCE-$FeCl_4$ may be a ferroelastic crystal. Ferroelastic phase transitions are typically accompanied by alterations in ferroelastic domains. A prevalent technique for investigating these domains is polarized light microscopy. Ferroelastic domains, when analyzed under orthogonally polarized light, exhibit distinct birefringence properties due to their different orientations, resulting in patterns characterized by alternating bright and dark regions. As illustrated in Fig. 3j, the thin film exhibits clear stripe-like ferroelastic domains within the ferroelastic phase, and the strip-shaped patterns are independent of the morphology of the thin film. During the heating process, the domain pattern remains stable in LTP. However, once the temperature exceeds T_{C1}, the ferroelastic domain pattern vanishes abruptly. This phenomenon occurs due to the paraelastic phase symmetry, which renders the crystal non-birefringent. Upon subsequent cooling, the crystal reverts to the ferroelastic phase, regaining its birefringence. Furthermore, the morphology of the crystal remains stable throughout this continuous heating and cooling process. In repeated cycles of high and low temperatures, ferroelastic domains can consistently disappear and reappear. DMCE-$FeCl_4$ is classified as a ferroelastic crystal belonging to the orthorhombic Aizu species 6*mmFmm*2. Spontaneous-strain components were calculated from the lattice parameters, yielding a significant spontaneous strain value of 0.0514. Details of the calculation process are provided in the ESI.†

The relationship between the structure and properties of matter is inherently intertwined. The origin of the ferroelasticity in DMCE-$FeCl_4$ is quite fascinating. Phase transitions in other similar systems usually follow the law of ferroelectric phase transitions but not ferroelastic phase transitions.[15,31,38] Clarifying the origin of phase transitions will help us design both ferroelectric and ferroelastic materials. By comparing the crystal structures of DMCE-$FeCl_4$, $[(CH_3)_4N][FeCl_4]$,[31] $[N(C_2H_5)_3CH_3][FeCl_4]$[38] and $[(CH_3)_3NCH_2Cl][FeCl_4]$,[15] we found that this type of material, overall, is an organic molecule surrounded by 8 $[FeCl_4]^-$ tetrahedral frameworks. In HTP, the cations rotate in the gaps of the $[FeCl_4]^-$ tetrahedral frameworks and are highly disordered. In LTP, the organic molecules become ordered or partly ordered. To investigate the interaction forces between molecules and $[FeCl_4]^-$ frameworks, we carried out an analysis using non-covalent interaction (NCI) calculations.[39,40] The scattered graph was generated by plotting sign(λ_2)ρ against the reduced density gradient (RDG). The following regions were defined based on the values of sign(λ_2)

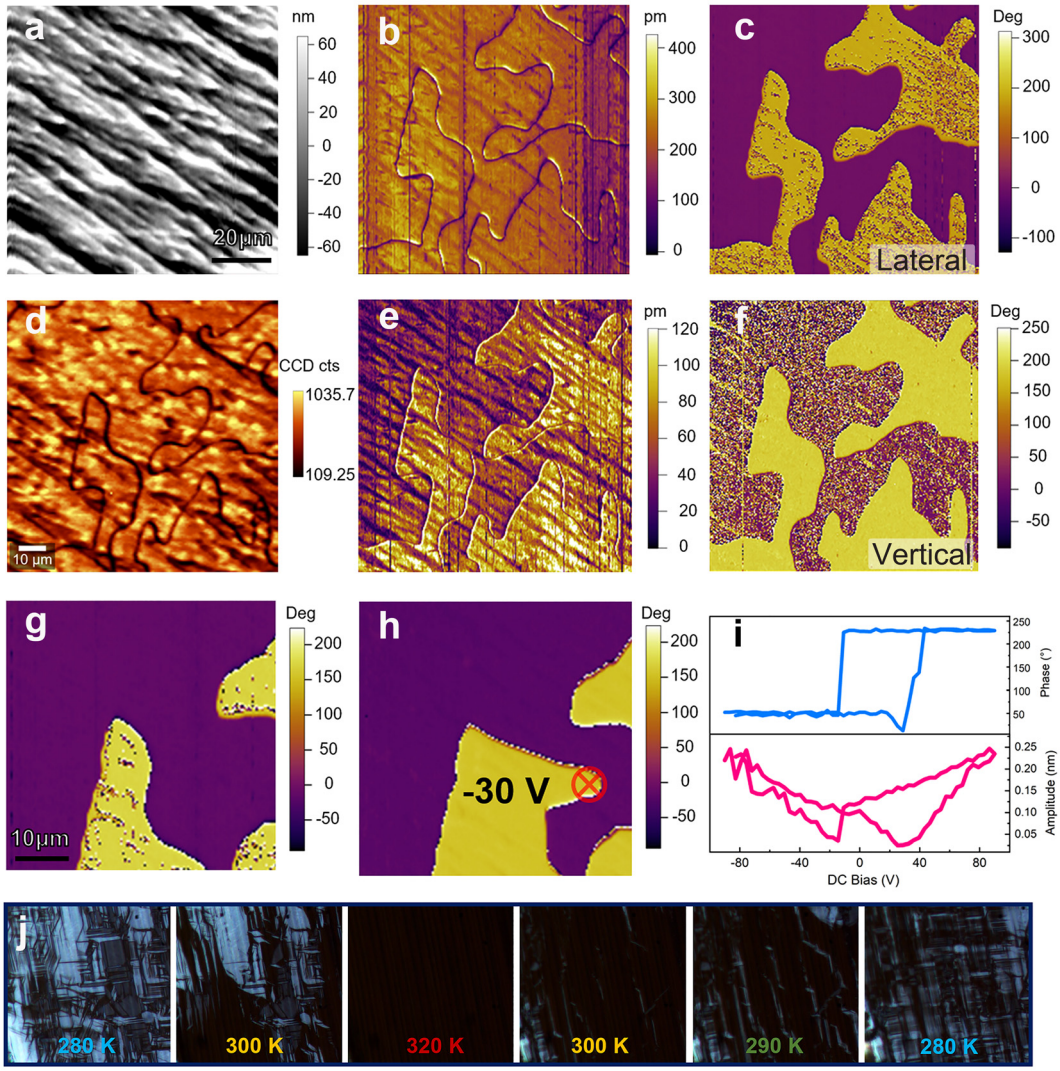

Fig. 3 Domain structure and domain switching of the DMCE-$FeCl_4$ thin film. (a) Topography image. Image size: 90 × 90 μm. (b) Lateral PFM amplitude and (c) phase images. (d) Scanning SHG image corresponding to ferroelectric domains. (e) Vertical PFM amplitude and (f) phase images in the same region. (g) Initial state of the lateral PFM phase image. Image size: 50 × 50 μm. (h) State after the first switching induced by poling with a DC tip bias of −30 V. (i) Phase hysteresis loop (up) and amplitude butterfly-shaped curve (down). (j) The evolution of the ferroelastic domain during the continuous heating and cooling process; the scale bar is 100 μm.

and ρ. Strong interactions, corresponding to halogen and hydrogen bonds, are characterized by $\rho > 0$ and $\lambda < 0$. Van der Waals interactions correspond to $\rho \approx 0$ and $\lambda \approx 0$. And strong repulsion, associated with the steric effect, correspond to $\rho > 0$ and $\lambda > 0$. The NCI analysis, as shown in Fig. 4c–f, indicated that the vast majority of the forces between the organic molecules and inorganic frameworks are van der Waals forces, regardless of whether there is halogen modification. The most obvious difference is that there are more steric hindrance effects and weak attraction in the organic molecules of DMCE-$FeCl_4$ than the others (for the contribution of each spike, see Fig. S7†). The sphericity[41] (S) values of the organic molecules are 0.923, 0.898, 0.908 and 0.864, respectively. As shown in Fig. 4g, the sphericity is positively correlated with the RDG minimum, indicating that the $[DMCE]^+$ cation, with smaller sphericity, has a stronger steric effect. Notably, the ferroelasticity did not correspond to the volume of each organic molecule (Fig. 4h).

Based on the above discussion, we propose that the shape of the molecule played an important role in the formation of the ferroelastic material. The steric hindrance effects caused the organic molecule to maintain asymmetry at a relatively high temperature. In contrast, quasi-spherical molecules can provide a certain polarity in an ordered state, which helps induce ferroelectricity in materials. However, due to their high symmetry, it is difficult to cause anisotropic deformation of the skeleton during the phase transition from HTP to LTP (Fig. 4a). Meanwhile, ellipsoidal molecules also approximate a spherical form in HTP, but as the temperature decreases, their inherent disorder is reduced. This reduction in disorder can readily trigger anisotropic stress within the lattices (Fig. 4b). Consequently, the material demonstrates

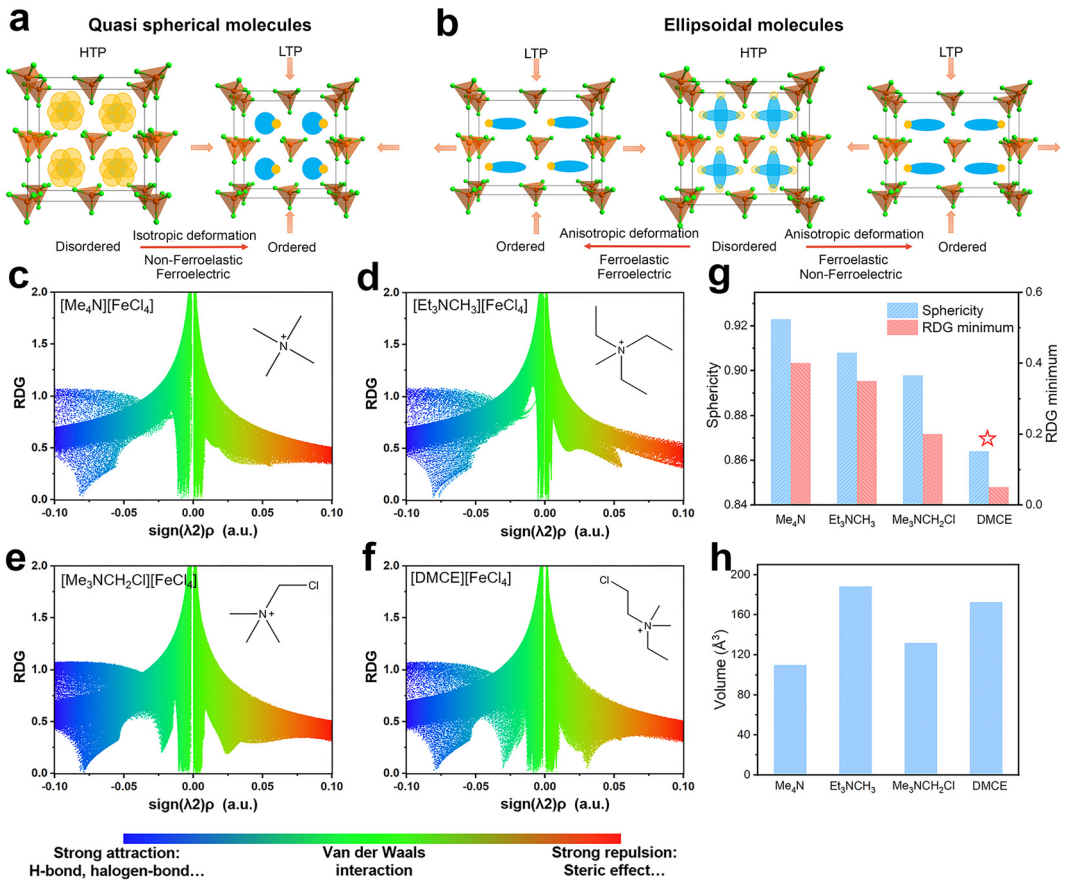

Fig. 4 Schematic diagram of the effect of the cation shape on the lattice structure in (a) ferroelectric and (b) ferroelastic materials. Non-covalent interaction (NCI) scatter diagrams of (c) $[Me_4N][FeCl_4]$, (d) $[Et_3NCH_3][FeCl_4]$, (e) $[Me_3NCH_2Cl][FeCl_4]$ and (f) $[Me_2EtNCH_3CH_2Cl][FeCl_4]$ (inset: the sphericity of each organic molecule). (g) The comparison of the sphericity and RDG minima of the above four organic molecules. (h) The comparison of the unit cell volume evolution of the above four organic molecules.

ferroelasticity, aligning with the characteristics of a ferroelastic phase transition.

Conclusion

In summary, by employing ferroelectrochemistry design strategies, we aimed to develop and synthesize materials exhibiting multiple ferroic phase transitions. The introduction of chlorine atoms and the ethyl group, in comparison with $(Me_4N)FeCl_4$, not only reduces the symmetry of the cations but also induces a steric effect between the cations and the anion frameworks. Based on this approach, we synthesized an organic–inorganic hybrid molecular ferroelectric DMCE-$FeCl_4$, which undergoes reversible ferroelectric and ferroelastic phase transitions at 299.9 K and 409.2 K, respectively. These transitions are primarily attributed to the thermal motion of $[DMCE]^+$ cations and the distortion and deformation of the $[FeCl_4]^-$ anion framework. The presence of switchable ferroelectric and ferroelastic domains strongly corroborates the existence of both ferroelectricity and ferroelasticity in this material. Furthermore, regarding magnetic properties, we predict that DMCE-$FeCl_4$ will exhibit magnetic rearrangement phenomena at very low temperatures. This work aims to achieve ferroic regulation through temperature, thereby advancing the exploration of multifunctional materials capable of multi-channel storage.

Author contributions

Jie Yao: data curation and writing – original draft; Zi-Jie Feng: data curation and validation; Jin-Qi Hu: formal analysis and validation; Guo-Wei Du: data curation; Yu-An Xiong: formal analysis and visualization; Hao-Ran Ji: formal analysis; Tai-Ting Sha: investigation; Xiangzhi Zhang: investigation; Zheng-Yin Jing: investigation; Qiang Pan: software and supervision; Huihui Hu: software and supervision; and Yu-Meng You: writing – review & editing and supervision.

Data availability

The experimental cif files can be found in CCDC (2380776–2380778†). The data supporting this article have been included as part of the ESI.†

Conflicts of interest

The authors declare no competing interests.

Acknowledgements

This work was supported by the National Key R&D Program of China (Grant No. 2021YFA1200700), the National Natural Science Foundation of China (Grant No. 21925502), and the Fundamental Research Funds for the Central Universities, China.

References

1 K. Aizu, A. Kumada, H. Yumoto and S. Ashida, Simultaneous ferroelectricity and ferroelasticity of $Gd_2(MoO_4)_3$, *J. Phys. Soc. Jpn.*, 1969, **27**, 511–511.
2 H.-Y. Zhang, C.-L. Hu, Z.-B. Hu, J.-G. Mao, Y. Song and R.-G. Xiong, Narrow band gap observed in a molecular ferroelastic: ferrocenium tetrachloroferrate, *J. Am. Chem. Soc.*, 2020, **142**, 3240–3245.
3 A. I. Khan, X. Marti, C. Serrao, R. Ramesh and S. Salahuddin, Voltage-Controlled Ferroelastic Switching in $Pb(Zr_{0.2}Ti_{0.8})O_3$ Thin Films, *Nano Lett.*, 2015, **15**, 2229–2234.
4 M. D. Hollingsworth, M. L. Peterson, K. L. Pate, B. D. Dinkelmeyer and M. E. Brown, Unanticipated Guest Motion during a Phase Transition in a Ferroelastic Inclusion Compound, *J. Am. Chem. Soc.*, 2002, **124**, 2094–2095.
5 Z. Sun, X. Wang, J. Luo, S. Zhang, D. Yuan and M. Hong, Ferroelastic phase transition and switchable dielectric behavior associated with ordering of molecular motion in a perovskite-like architectured supramolecular cocrystal, *J. Mater. Chem. C*, 2013, **1**, 2561–2567.
6 S. H. Baek, H. W. Jang, C. M. Folkman, Y. L. Li, B. Winchester, J. X. Zhang, Q. He, Y. H. Chu, C. T. Nelson, M. S. Rzchowski, X. Q. Pan, R. Ramesh, L. Q. Chen and C. B. Eom, Ferroelastic switching for nanoscale non-volatile magnetoelectric devices, *Nat. Mater.*, 2010, **9**, 309–314.
7 Q.-W. He, J.-H. Wang, D.-Y. Zhu, D.-S. Tang, Z. Lv, F. Guo and X.-C. Wang, Strong Vertical Piezoelectricity and Broad-pH-Value Photocatalyst in Ferroelastic Y_2Se_2BrF Monolayer, *Nano Lett.*, 2024, **24**, 8979–8987.
8 W. Lei, R. Hu, S. Han, H. Yuan, W. Jiao, Y. Luo and H. Liu, Directional Control of the Electronic and Phonon Transport Properties in the Ferroelastic $PtSe_2$, *J. Phys. Chem. C*, 2023, **128**, 543–548.
9 X. Ding and E. Salje, Heat transport by phonons and the generation of heat by fast phonon processes in ferroelastic materials, *AIP Adv.*, 2015, **5**, 053604.
10 E. K. Salje, Multiferroic domain boundaries as active memory devices: trajectories towards domain boundary engineering, *ChemPhysChem*, 2010, **11**, 940–950.
11 P. Gao, J. Britson, C. T. Nelson, J. R. Jokisaari, C. Duan, M. Trassin, S.-H. Baek, H. Guo, L. Li, Y. Wang, Y.-H. Chu, A. M. Minor, C.-B. Eom, R. Ramesh, L.-Q. Chen and X. Pan, Ferroelastic domain switching dynamics under electrical and mechanical excitations, *Nat. Commun.*, 2014, **5**, 3801.
12 V. Nagarajan, A. Roytburd, A. Stanishevsky, S. Prasertchoung, T. Zhao, L.-Q. Chen, J. Melngailis, O. Auciello and R. Ramesh, Dynamics of ferroelastic domains in ferroelectric thin films, *Nat. Mater.*, 2003, **2**, 43–47.
13 Z. Sun, X. Liu, T. Khan, C. Ji, M. A. Asghar, S. Zhao, L. Li, M. Hong and J. Luo, A photoferroelectric perovskite–type organometallic halide with exceptional anisotropy of bulk photovoltaic effects, *Angew. Chem., Int. Ed.*, 2016, **55**, 6545–6550.
14 J.-X. Gao, W.-Y. Zhang, Z.-G. Wu, Y.-X. Zheng and D.-W. Fu, Enantiomorphic perovskite ferroelectrics with circularly polarized luminescence, *J. Am. Chem. Soc.*, 2020, **142**, 4756–4761.
15 D. Li, X.-M. Zhao, H.-X. Zhao, L.-S. Long and L.-S. Zheng, Coexistence of Magnetic-Optic-Electric Triple Switching and Thermal Energy Storage in a Multifunctional Plastic Crystal of Trimethylchloromethyl Ammonium Tetrachloroferrate(III), *Inorg. Chem.*, 2019, **58**, 655–662.
16 Z. Sun, J. Luo, T. Chen, L. Li, R. G. Xiong, M. L. Tong and M. Hong, Distinct Molecular Motions in a Switchable Chromophore Dielectric 4—N, N–Dimethylamino–4′–N′–methylstilbazolium Trifluoromethanesulfonate, *Adv. Funct. Mater.*, 2012, **22**, 4855–4861.
17 H.-Y. Zhang, Y.-Y. Tang, P.-P. Shi and R.-G. Xiong, Toward the targeted design of molecular ferroelectrics: modifying molecular symmetries and homochirality, *Acc. Chem. Res.*, 2019, **52**, 1928–1938.
18 Q.-Q. Jia, G. Teri, J.-Q. Luo, H.-F. Ni, P.-Z. Huang, M.-M. Lun, Z.-X. Zhang, Y. Zhang and D.-W. Fu, Experimental Observation of the Fully Ferroelectric–Fully Ferroelastic Effect in Multiferroic Hybrid Perovskites, *J. Am. Chem. Soc.*, 2024, **146**, 21120–21128.
19 Y.-M. You, W.-Q. Liao, D. Zhao, H.-Y. Ye, Y. Zhang, Q. Zhou, X. Niu, J. Wang, P.-F. Li and D.-W. Fu, An organic-inorganic perovskite ferroelectric with large piezoelectric response, *Science*, 2017, **357**, 306–309.
20 W. Zhang and R.-G. Xiong, Ferroelectric Metal–Organic Frameworks, *Chem. Rev.*, 2012, **112**, 1163–1195.
21 P.-P. Shi, Y.-Y. Tang, P.-F. Li, W.-Q. Liao, Z.-X. Wang, Q. Ye and R.-G. Xiong, Symmetry breaking in molecular ferroelectrics, *Chem. Soc. Rev.*, 2016, **45**, 3811–3827.
22 E. Salje, Phase transitions in ferroelastic and co-elastic crystals, *Ferroelectrics*, 1990, **104**, 111–120.
23 Y.-L. Zeng, Y. Ai, S.-Y. Tang, X.-J. Song, X.-G. Chen, Y.-Y. Tang, Z.-X. Zhang, Y.-M. You, R.-G. Xiong and H.-Y. Zhang, Axial-Chiral BINOL Multiferroic Crystals with Coexistence of Ferroelectricity and Ferroelasticity, *J. Am. Chem. Soc.*, 2022, **144**, 19559–19566.
24 K. Aizu, Possible Species of "Ferroelastic" Crystals and of Simultaneously Ferroelectric and Ferroelastic Crystals, *J. Phys. Soc. Jpn.*, 1969, **27**, 387–396.

25 K. Aizu, Determination of the state parameters and formulation of spontaneous strain for ferroelastics, *J. Phys. Soc. Jpn.*, 1970, **28**, 706–716.
26 C. Chen, S. Gao, W. Song, H. Li, S.-N. Zhu and T. Li, Metasurfaces with Planar Chiral Meta-Atoms for Spin Light Manipulation, *Nano Lett.*, 2021, **21**, 1815–1821.
27 M. Liu, W. Zhu, P. Huo, L. Feng, M. Song, C. Zhang, L. Chen, H. J. Lezec, Y. Lu, A. Agrawal and T. Xu, Multifunctional metasurfaces enabled by simultaneous and independent control of phase and amplitude for orthogonal polarization states, *Light: Sci. Appl.*, 2021, **10**, 107.
28 N. W. Hendrickx, L. Massai, M. Mergenthaler, F. J. Schupp, S. Paredes, S. W. Bedell, G. Salis and A. Fuhrer, Sweet-spot operation of a germanium hole spin qubit with highly anisotropic noise sensitivity, *Nat. Mater.*, 2024, **23**, 920–927.
29 K. Kang, B. Shen, Y. Qiu, Y. Zeng, Z. Xia, K. Watanabe, T. Taniguchi, J. Shan and K. F. Mak, Evidence of the fractional quantum spin Hall effect in moiré $MoTe_2$, *Nature*, 2024, **628**, 522–526.
30 A. I. Kuznetsov, M. L. Brongersma, J. Yao, M. K. Chen, U. Levy, D. P. Tsai, N. I. Zheludev, A. Faraon, A. Arbabi and N. Yu, Roadmap for optical metasurfaces, *ACS Photonics*, 2024, **11**, 816–865.
31 J. Harada, N. Yoneyama, S. Yokokura, Y. Takahashi, A. Miura, N. Kitamura and T. Inabe, Ferroelectricity and Piezoelectricity in Free-Standing Polycrystalline Films of Plastic Crystals, *J. Am. Chem. Soc.*, 2018, **140**, 346–354.
32 D. Li, X.-M. Zhao, H.-X. Zhao, X.-W. Dong, L.-S. Long and L.-S. Zheng, Construction of Magnetoelectric Composites with a Large Room-Temperature Magnetoelectric Response through Molecular–Ionic Ferroelectrics, *Adv. Mater.*, 2018, **30**, 1803716.
33 X.-N. Hua, W.-Q. Liao, Y.-Y. Tang, P.-F. Li, P.-P. Shi, D. Zhao and R.-G. Xiong, A room-temperature hybrid lead iodide perovskite ferroelectric, *J. Am. Chem. Soc.*, 2018, **140**, 12296–12302.
34 W.-Q. Liao, Y. Zhang, C.-L. Hu, J.-G. Mao, H.-Y. Ye, P.-F. Li, S. D. Huang and R.-G. Xiong, A lead-halide perovskite molecular ferroelectric semiconductor, *Nat. Commun.*, 2015, **6**, 7338.
35 J. Yao, Z.-J. Feng, Z. Hu, Y.-A. Xiong, Q. Pan, G.-W. Du, H.-R. Ji, T.-T. Sha, J. Lu and Y.-M. You, 2D Molecular Ferroelectric with Large Out-of-plane Polarization for In-Memory Computing, *Adv. Funct. Mater.*, 2024, **34**, 2314790.
36 S. Farokhipoor and B. Noheda, Conduction through 71° Domain Walls in $BiFeO_3$ Thin Films, *Phys. Rev. Lett.*, 2011, **107**, 127601.
37 A. J. Lehner, D. H. Fabini, H. A. Evans, C.-A. Hébert, S. R. Smock, J. Hu, H. Wang, J. W. Zwanziger, M. L. Chabinyc and R. Seshadri, Crystal and Electronic Structures of Complex Bismuth Iodides $A_3Bi_2I_9$ (A = K, Rb, Cs) Related to Perovskite: Aiding the Rational Design of Photovoltaics, *Chem. Mater.*, 2015, **27**, 7137–7148.
38 S. Burazer, J. Popović, Z. Jagličić, M. Jagodič, A. Šantić, A. Altomare, C. Cuocci, N. Corriero and M. Vrankić, Magnetoelectric Coupling Springing Up in Molecular Ferroelectric: $[N(C_2H_5)_3CH_3][FeCl_4]$, *Inorg. Chem.*, 2020, **59**, 6876–6883.
39 T. Lu, A comprehensive electron wavefunction analysis toolbox for chemists, Multiwfn, *J. Chem. Phys.*, 2024, **161**, 082503.
40 E. R. Johnson, S. Keinan, P. Mori-Sánchez, J. Contreras-García, A. J. Cohen and W. Yang, Revealing Noncovalent Interactions, *J. Am. Chem. Soc.*, 2010, **132**, 6498–6506.
41 H. Wadell, Volume, Shape, and Roundness of Quartz Particles, *J. Geol.*, 1935, **43**, 250–280.